Appl. Phys. B 62, 389–397 (1996)

Applied Physics B Lasers and Optics

Split-step Fourier methods applied to model nonlinear refractive effects in optically thick media

J.M. Burzler*, S. Hughes, B.S. Wherrett**

Department of Physics, Heriot-Watt University, Edinburgh EH14 4AS, UK
(Fax: +44-131/451-3136, E-mail: PHYBSW@phyfs1.phy.hw.ac.uk)

Received: 9 June 1995 / Accepted: 7 September 1995

Abstract. We describe and example the Beam Propagation Method (BPM) used to model and simulate nonlinear refractive and absorptive effects in materials with applications to optical limiting and switching. Various scenarios including laser-beam trapping and laser-beam division are investigated, in order to demonstrate the power of the BPM. A novel technique is also described for efficiently modelling the external far-field propagation from nonlinear media, including the propagation of non-Gaussian-shaped spatial profiles. The methods are finally combined with the phenomenon of nonlinear absorption to demonstrate enhanced power limiting in the presence of self-refraction. Optimal parameters for high-fluence power-limiting are subsequently discussed.

PACS: 02.60.Cb; 02.70.–c; 42.10; 42.25.Bs; 42.65

It is well established that materials exhibiting a rapidly responding nonlinear refractive index can be exploited in optical limiting [1–4] and high-speed optical switching [5, 6]. In this paper, we employ Fast Fourier Transforms (FFTs) to model quantitatively the effect of such nonlinear refraction in both 'optically' thin and thick media. In thin media, an incident Gaussian beam, for example, is taken to experience a change in phase profile on propagation through the material, but remains of Gaussian amplitude profile. In thick media, it is necessary to determine both the phase and amplitude profiles at the material exit face due to the influence of nonlinear refraction (and nonlinear absorption) on the beam propagating through the medium. The Beam Propagation Method (BPM) [7–11] allows this to be achieved efficiently. Further, a novel technique for simulating the subsequent external propagation from the media is described; a single discrete fast Fourier transform is used.

* *Present address:* Institut für Angewandte Physik, Universität Regensburg, D-93040 Regensburg, Germany (FAX: +49-941/943/4223, E-mail: Josef.Burzler@physik.uni-regensburg.de)

** *Present address:* Department of Physics and Materials Sciences Center, Philipps Universität, D-35032 Marburg, Germany (Fax: +49-6421/28-7076, E-mail: hughes@ax1311.physik.uni-marburg.de)

For modelling electromagnetic-field propagation in optical fibres, the BPM [7–11] has been employed extensively; sometimes referred to as the split-step FFT method, it is a well-known, robust computational technique. The BPM is particularly suited for propagation over small distances, and consequently it is an excellent choice for describing the propagation through materials for application to power limiting and optical switching ([12, 13], for example).

Following a description of the theoretical techniques, various examples are presented in this paper. These include the propagation of non-Gaussian spatial profiles, laser-beam trapping, and Gaussian-beam-profile division. Finally, an analysis is presented of enhanced optical limiting by cascading the effects of nonlinear refraction with induced absorption. Optimal parameters for optical limiting are presented for the case of a reverse saturable absorber (induced-absorptive dye) [14–16].

1 Theoretical techniques

In this section, numerical techniques are discussed for propagating an electric field E, with three spatial coordinates and a time dependence, through optically thick and thin media. The nonlinear refraction is handled from a diffractive point of view, i.e., dispersion effects are ignored, and in the first few examples a continuous wave (cw) beam is assumed. The time dependence, needed for pulse propagation analysis, is employed in the final section to describe enhanced power limiting, where the nonlinear absorption contributions are calculated using rate equations. The refractive and absorptive nonlinearities are handled in a self-consistent manner.

In essence, the three-dimensional BPM [8, 17] relates the electric field inside the medium at an axial position $z + \Delta z$ to that of the electric field at z; it is based on the following expression:

$$E(x, y, z + \Delta z, t) = \hat{\mathrm{P}}\,\hat{\mathrm{A}}\,\hat{\mathrm{L}}\,\hat{\mathrm{A}}\,\hat{\mathrm{P}}\,E(x, y, z, t)\,, \tag{1}$$

where the various operators are discussed below. A schematic of the numerical routine is shown in Fig. 1, which depicts the BPM as equivalent to progressing the light field through a periodic array of optical lenses, where the strength of each lens depends on the local nonlinearity.

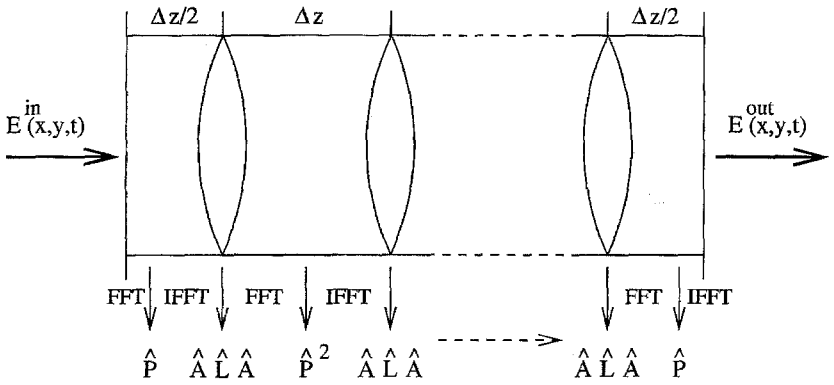

Fig. 1. Schematic diagram for the BPM (see text) and showing how the nonlinear material may be viewed as a series of nonlinear lenses. FFT represents a Fast Fourier Transform and the input and output fields are respectively labelled, $E^{\text{in}}(x, y, t)$ and $E^{\text{out}}(x, y, t)$

The propagation operator ($\widehat{\text{P}}$) is defined by [8]:

$$\widehat{\text{P}} = \exp\left(\text{i}k_0 n_0 \Delta z/2\right) \times \exp\left[\text{i}\frac{\Delta z}{2}\left(\frac{\nabla_t^2}{(\nabla_t^2 + n_0^2 k_0^2)^{1/2} + n_0 k_0}\right)\right], \quad (2)$$

which originates simply from the solution of the wave equation in a homogeneous medium for propagation through a distance $\Delta z/2$. Here, n_0 and k_0 are the linear refractive index and wave vector, respectively. The execution of this operator is carried out in the spatial Fourier domain. The electric field $E(x, y, z, t)$ which is given on a discrete $N_x \times N_y$ grid is written as a finite Fourier series

$$E(x, y, z, t) = \sum_r \sum_s E_{rs}(z, t) \exp(\text{i}k_{xr}x) \exp(\text{i}k_{ys}y) . \quad (3)$$

The transverse derivative ∇_t^2 may then be expressed for each component as

$$\nabla_t^2 \equiv -(k_{xr}^2 + k_{ys}^2) , \quad (4)$$

where k_{xr} and k_{ys} ($\ll n_0 k_0$) are the spatial frequencies of the two-dimensional Fourier series, which are computed using a FFT. Thus, the propagation operator acts on the discrete 2-D Fourier components of the electric field, $E_{rs}(z, t)$. The use of finite Fourier transforms gives periodic boundary conditions to the computational grid.

The optical properties in the medium of interest are not constant but generally vary with the irradiance I of the light field and with time t. The refractive index $n = n_0 + \Delta n(I)$ is described in terms of the linear refractive index n_0 perturbed by a small index change Δn; an absorption may also be included by using a absorption coefficient $\alpha_{\text{nl}} = \alpha_0 + \Delta\alpha(I)$, which is discussed in Sect. 4.

After the propagation via (3), the electric field is transformed back into real space where the nonlinearities are included. Firstly, the field is multiplied by an attenuation operator (Fig. 1)

$$\widehat{\text{A}} = \exp\left(-\frac{\alpha_{\text{nl}}}{4}\Delta z\right) , \quad (5)$$

which accounts for the absorption, and then by the lens operator,

$$\widehat{\text{L}} = \exp\left[\text{i}\frac{k_0 n_0}{2}\int_z^{z+\Delta z}\left(\frac{n^2(x, y, z', t)}{n_0^2} - 1\right) \text{d}z'\right] . \quad (6)$$

The attenuation operator $\widehat{\text{A}}$ is applied a second time. The operators $\widehat{\text{A}}$ and $\widehat{\text{L}}$ are calculated using the trapezoidal rule, which is a rigorous approximation for small Δz. Finally, the field is again transformed into Fourier space and propagated using the propagation operator $\widehat{\text{P}}$. Physically, an input field traverses a distance $\Delta z/2$ through the nonlinear absorbing medium; the field then passes through a nonlinear lens and as such has its phase modified; propagating through a further $\Delta z/2$ slice the magnitude is modified, which in turn alters the phase again, and so on.

The computational time required for the entire propagation simulation is inversely proportional to the stepwidth Δz. Typically, for modelling waveguide structures [9, 10], where the transverse changes in the refractive index are large, very small step sizes are required. However, since here the changes in the nonlinear refractive index are comparatively small, the chosen step size can be relatively large for our purposes; a typical value is $\simeq 0.1$ mm. One can therefore propagate a beam through typical nonlinear sample lengths ($0.05 - 1$ cm) in only a few steps. Furthermore, all the 2-D Fourier transforms are performed with high efficiency using a FFT algorithm (2D-FFT), which requires a computational time approximately proportional to $N_x N_y \log(N_x N_y)$, where $N_x \times N_y$ is the size of the computational grid. The number of grid points is consequently the most important factor in determining the overall computation time. Typical applications with smooth input profiles and moderate nonlinear effects require only 64×64 to 256×256 grid points for accurate simulations.

Having a method to simulate the beam propagation through a nonlinear medium, one is often also interested in the resulting external (far-field) diffraction patterns from such a medium. This involves calculating the linear propagation from a given input field. Theoretical propagation methods such as a straightforward integration of the Huygens-Fresnel diffraction [2, 18] integral are often used, but are computationally inefficient and usually require a computation time of the order of $\simeq N_x^2 N_y^2$. Algorithms such as the fast Hankel transform [19] or the Gaussian decomposition method [20] can be a better choice. However, these methods are restricted to cases where the beams have circular or elliptic symmetry.

A simple method is employed here which allows us to simulate quite arbitrarily shaped spatial profiles while having an efficiency comparable to that of the fast Hankel transform

methods. It is based on the Fresnel approximation of the Fresnel-Kirchoff diffraction formula:

$$E(x', y', z_2, t) = s(x', y', d) \times \int\int_{-\infty}^{\infty} \exp\left[-\mathrm{i}\frac{2\pi}{d\lambda}\left(x'x + y'y\right)\right] f(x, y, z_1, d, t)\,\mathrm{d}x\,\mathrm{d}y \;, \quad (7)$$

where

$$s(x', y', d) = -\frac{\mathrm{i}}{\lambda d}\exp(\mathrm{i}kd)\exp\left[\mathrm{i}\frac{2\pi}{2d\lambda}\left(x'^2 + y'^2\right)\right] \;, \quad (8)$$

and

$$f(x, y, z_1, d, t) = \exp\left[\mathrm{i}\frac{2\pi}{2d\lambda}\left(x^2 + y^2\right)\right] E(x, y, z_1, t) \;. \quad (9)$$

This is valid within the Fresnel approximation even for small distances $d = z_2 - z_1$ between a detector plane (far-field) at the position z_2 and the sample exit plane at z_1.

The double integral in (7) is in the same form as a Fourier integral. The general case of solving such Fourier-like integrals has been discussed elsewhere [21] for one dimension, it involves the concept of fractional Fourier transforms. This general formalism could be extended to two dimensions. However, it has become apparent during our work that for almost all realistic applications a much simpler and more efficent method can be used to compute the 2-D integrals, by transforming them into a single 2-D discrete Fourier transform.

In the Fresnel-Kirchoff diffraction formula (7), the input field $E(x, y, z_1, t)$ at the diffraction plane and the output field $E(x, y, z_2, t)$ at the detector plane are evaluated at points on a discrete $N_x \times N_y$ grid as in the BPM. The grid points of the input field are equally spaced by Δx and Δy in the transverse spatial directions x and y, respectively; their abscissas are defined through $x_j = \Delta x j$ with $j = (-N_x/2 \ldots N_x/2 - 1)$ and analogously for y. Thus, the grid covers an area with the dimensions $L_x \times L_y$, where $L_x = N_x \Delta x$ and $L_y = N_y \Delta y$. The spacing and the grid points of the output field are defined in a similar manner; the output-grid parameters are primed.

With these definitions, one can transform the 2-D integration in the Fresnel equation into a double sum

$$E(x'_m, y'_n, z_2, t) = s(x'_m, y'_n, d) \times \Delta x \Delta y \sum_j \sum_l \exp\left[-\mathrm{i}\frac{2\pi}{d\lambda}\left(mj\Delta x'\Delta x + nl\Delta y'\Delta y\right)\right] \times f(x_j, y_l, z_1, d, t) \;, \quad (10)$$

which becomes a discrete 2-D Fourier transform if the conditions

$$N_x \Delta x \Delta x' = N_y \Delta y \Delta y' = d\lambda \quad (11)$$

are fulfilled. For most practical cases, this condition is relatively easy to achieve. Typically, one would adjust the spacings Δx and Δy of the input grid so that the area $L_x \times L_y$ incorporates almost all of the pulse energy. The spacings of the output grid $\Delta x'$ and Δy are then determined by (11). This is usually no problem since it gives an area of the output grid with reasonable dimensions L'_x and L'_y. In order to check the consistency of the method it was first applied to the linear propagation of a Gaussian beam, for which the analytic result is well known. We simulate for a Gaussian beam with $\lambda = 532\,\mu$m, and a spot size of $90\,\mu$m (HW e^{-2} maximum irradiance), propagating from the focal plane to a distance of 50 cm; using a computational grid with a size of only 32×32 and areas $L_x, L_y = 450\,\mu$m, $L'_x, L'_y = 5.4$ mm resulted in a relative error compared to the analytic solution that is smaller than one part in 10^9 at the beam centre region, both in amplitude and phase. The CPU time needed for the simulation was 2 s on a SUN Sparc-Station 5. An application adopting this algorithm has been presented by us elsewhere for modelling z-scan measurements [22], allowing one accurately and efficiently to determine nonlinear refractive coefficients by fitting to experimental data.

2 Non-Gaussian-shaped spatial profiles propagating through linear and nonlinear media

As an initial example, consider the spatial patterns arising from the linear propagation of a plane-wave, cw field, that is incident on an equilateral triangular aperture with side lengths $100\,\mu$m. With an input wavelength of 532 nm, the subsequent diffraction patterns are shown in Fig. 2 as the beam propagates various distances from the aperture. This remarkable display of the diffraction patterns can be computed very quickly (in less than 10 s on a SUN Sparc-Station 5 for a 256×256 grid) using the external propagation technique outlined above, where a single 2-D FFT is employed for each propagation distance. As can be seen, diffraction distorts the input field which initiates patterns to form in the near field; further propagation causes the triangular profile to be inverted since diffractive effects are stronger at the edges, 1 cm away. Finally, in Fig. 2, at a propagation distance of 1 m, the spatial pattern has 6-fold rotational symmetry as is known from the 'exact' Fraunhofer field distribution. Note that the transverse dimensions increase from about 0.1 mm to 1.4 mm for a propagation of 1 m. The above-described method is approximately seven hundred times faster than computation by performing a numerical integration of the diffraction formula.

Next, consider the case where an input cw Gaussian beam, $\lambda = 532$ nm, with a spot size $\omega_0 = 90\,\mu$m (HW e^{-2} maximum irradiance) and a peak irradiance of $1\,\mathrm{GW/cm^2}$ is focused onto a triangular aperture of side-lengths $100\,\mu$m, which is situated in front of a 6 mm nonlinear sample with a focusing nonlinearity. In this analysis, the change in refractive index within the focusing material Δn, modelled by an instantaneous Kerr-like term, i.e.,

$$\Delta n(x, y, z', t) = n_2 I(x, y, z', t) \;, \quad (12)$$

where $I = c n_0 \epsilon_0 |E|^2/2$ is the irradiance of the light field. A linear refractive index $n_0 = 1.65$ and a nonlinear index $n_2 = 3.6 \times 10^{-14}\,\mathrm{W^{-1}cm^2}$ are assumed; these are comparable with the values of the solvent CS_2 [23]. The input-beam profile is depicted in Fig. 3a and the simulated output field at the sample exit is shown in Fig. 3b. Apart from experiencing strong self-focusing within the sample ($90\,\mu$m to $\simeq 10\,\mu$m), the spatial beam also separates into three separate profiles. This breakup is induced by the anisotropy of the input field, caused by the triangular aperture. Interestingly, the optical

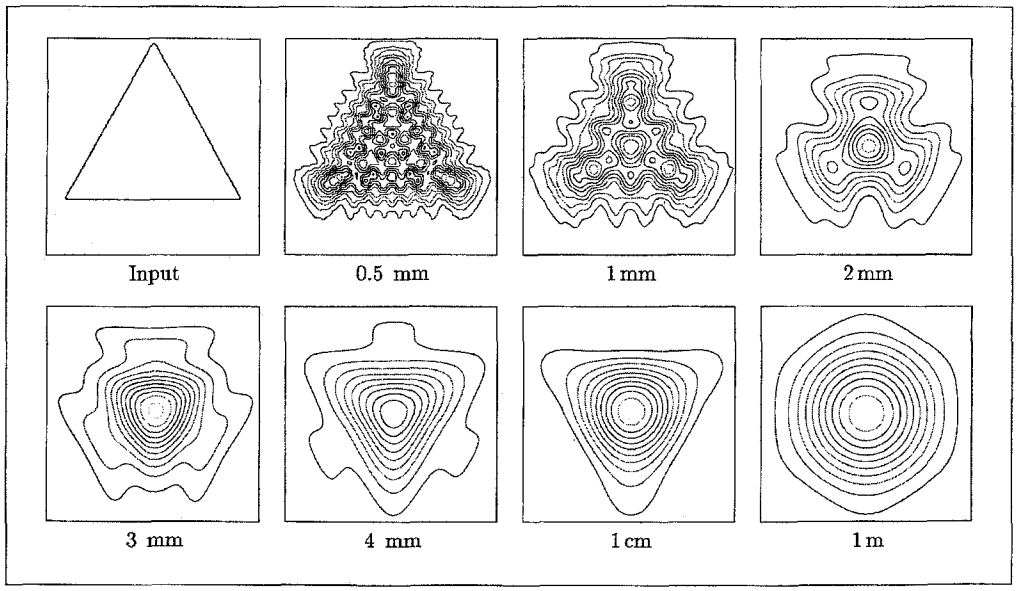

Fig. 2. Diffraction patterns from a 0.1 mm side length equilateral triangular aperture, depicting the near- and far-field patterns as the beam propagates the distances: 0.5; 1; 2; 3; 4 mm; 1 cm; and 1 m. Eventually, a smooth hexagonal profile is formed in the far field

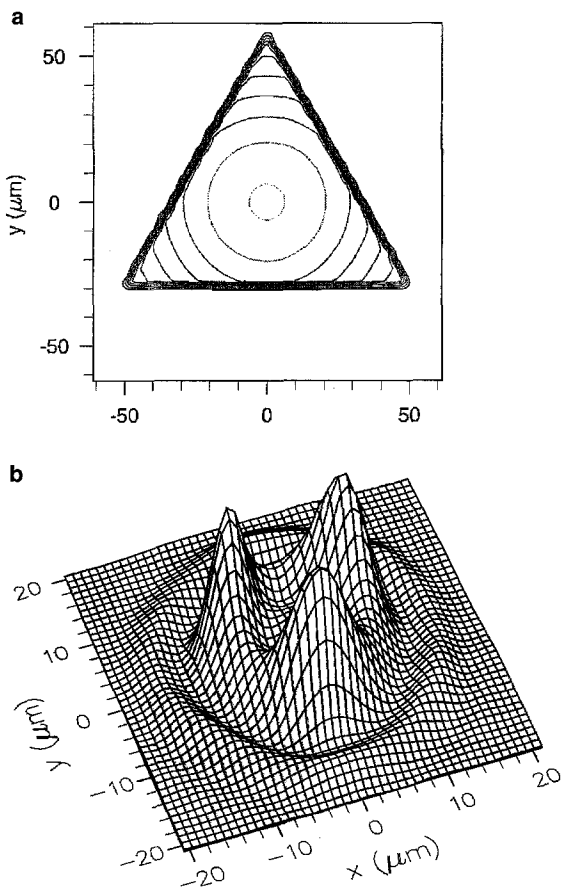

Fig. 3. a An input Gaussian beam profile, with a spotsize $\omega_0 = 90\,\mu$m (HW e^{-2} maximum irradiance) focused onto a triangular aperture of side-lengths $100\,\mu$m, which is taken to be situated in front of a 6 mm nonlinear sample with a focusing nonlinearity (see text). **b** 3-D plot of the resulting profile of the output irradiance (6 mm propagation distance), assuming a nonlinear refractive index of $3.6 \times 10^{-14}\,\mathrm{W^{-1}cm^2}$ and an input peak irradiance of $1\,\mathrm{GW/cm^2}$

thickness of the sample is only 0.21 in units of the Rayleigh range (diffraction length). Note, upon subsequent propagation into the far-field, the beam is split into four strong spots, and weaker peaks. Throughout the simulations, the power of the beam is conserved, as expected since absorption is ignored.

3 Laser-beam trapping and spatial beam division: Self-focusing and self-defocusing

At sufficient input irradiance, spatially positive nonlinear refractive effects may cause a laser beam to become trapped [24, 25] as the effects of nonlinear focusing compensate the spreading due to diffraction. In contrast, a negative nonlinear refractive index can cause a single input spatial beam to divide into two separate profiles [26]. Figure 4a depicts an example of the trapping case for a 532 nm Gaussian laser beam with an input spot-size $\omega_0 = 60\,\mu$m. The peak input irradiance I_0 is $9 \times 10^9\,\mathrm{W/cm^2}$ and the material is assumed to have a nonlinear refractive index $n_2 = 7 \times 10^{-16}\,\mathrm{W^{-1}cm^2}$ and a linear refractive index of 1.33; this corresponds to the Kerr solvent methanol [27]. Initially, positive refractive-index changes induce self-focusing which causes the spot size to reduce and the centre irradiances to increase; consequently, further refractive index changes are induced and sufficient nonlinearities and sample length suffice to keep the beam trapped. In the absence of nonlinear refraction, i.e., at low irradiances, the resulting beam-profile evolution is markedly different, as can be seen in Fig. 4b.

To example self-defocusing, an elliptic Gaussian beam propagating through an isotropic nonlinear medium is simulated. The irradiance profile is

$$I = I_0 \exp\left[-\left(\frac{2x}{\omega_{0x}}\right)^2 - \left(\frac{2y}{\omega_{0y}}\right)^2\right], \qquad (13)$$

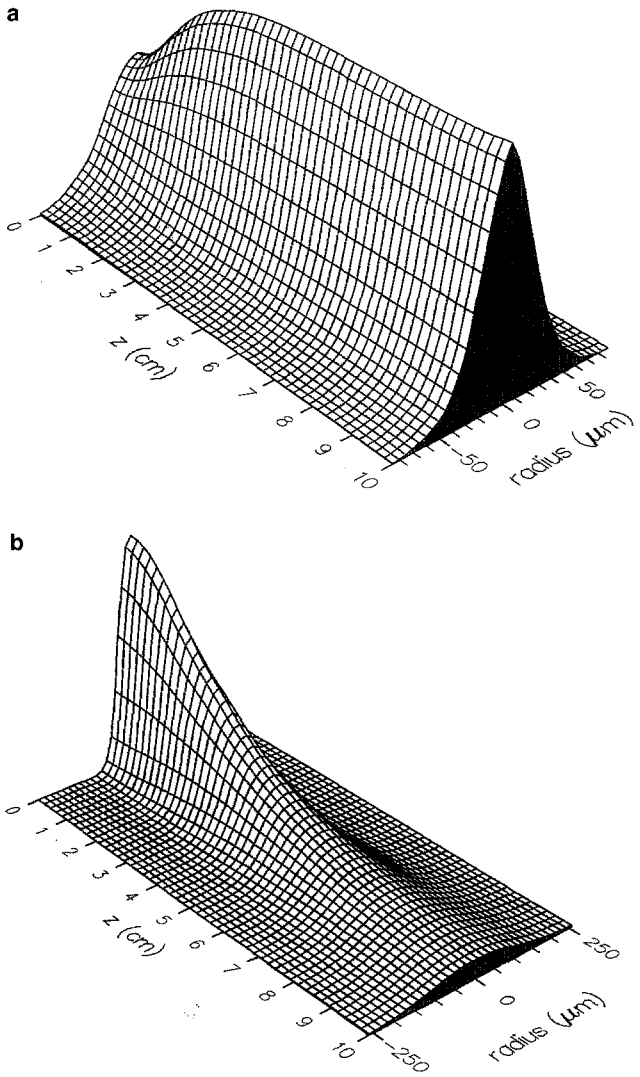

Fig. 4. a Demonstration of laser trapping whereby the self-focusing nonlinearities are sufficient to overcome the spreading effects due to diffraction and the focused spatial profile of the beam remains throughout the nonlinear medium. **b** The evolution of input spatial profile, but without the inclusion of any nonlinearities, i.e., $n_2 = 0$. The beam is seen to spread out due to refraction as it propagates in the z-direction

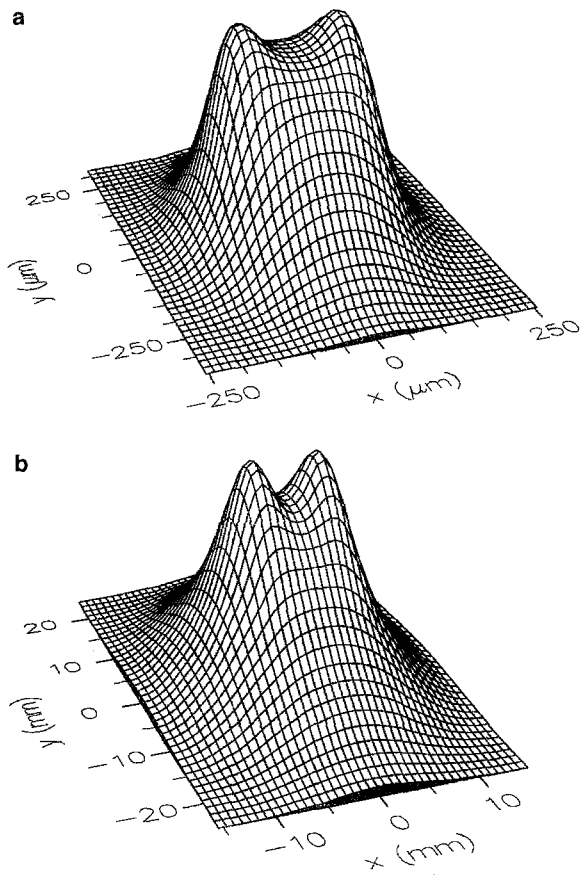

Fig. 5. a 2-D contour plot for an elliptic input profile distorted at the sample exit, for a 1 cm nonlinear path length. The beam is seen to split into two separate spatial profiles due to the self-defocusing. **b** The subsequent far-field profile after an external propagation of 50 cm; further distortions of the original input elliptical beam are shown

where the spotsizes in x- and y-direction ω_{0x} and ω_{0y} are taken to be 40 and 20 μm, respectively. An input irradiance of 6 W/cm^2 is assumed, focused onto the surface of a 1 cm thick nonlinear homogeneous medium with a linear refractive index $n_0 = 1.5$ and a nonlinear refraction index of $n_2 = -1 \times 10^{-4}\,\mathrm{W}^{-1}\mathrm{cm}^2$. The calculated output-beam profile at the sample exit is shown in Fig. 5a, demonstrating the division of the beam as a result of self-defocusing. This beam was further propagated to a detector plane 50 cm away from the material, where further distortions result in the profile shown in Fig. 5b, showing two spatially distinct peaks. This result is quite different to that obtained by Harvey et al. [28] for the case of a thin sample in that here a division of the beam is achieved both inside the sample and in the far field. In the thin sample approximation a division in the far field can only be achieved for beams propagating through an anisotropic material. For thick samples, an anisotropy in the homogeneous material is created by the optical anisotropy of the elliptical beam.

4 Enhanced power limiting by combining nonlinear absorption with the effects of nonlinear refraction

The final example presented is for the case of passive optical limiting of short pulses [1–4]. Obvious applications involve the safeguard of sensors and sensitive optical components (for example, the human eye). From an absorptive point of view, semiconductors can exhibit such behavior by utilizing either two-photon absorption or free-carrier absorption [4, 29]. In dyes, current interest for ultrafast limiting systems concentrates on Reverse Saturable Absorbers (RSAs) [14–16, 30–32] which have an excited-state absorption cross section that is larger than the ground-state absorption cross section. The latter will be modelled here; they offer the advantages of a broad spectral range and high damage thresholds, in addition to ultrafast response times which result from the electronic origin of the nonlinearity. The techniques which follow may be applied just as easily to the semiconductor case.

At certain wavelengths, the build up in population in an excited state at high incident irradiances leads to an increase

of the absorption coefficient (induced absorption), and optical limiting can be achieved. This occurs if the cross section of the excited species is sufficently larger than that of the ground-state species so that induced absorption overcomes the effect of saturation. The induced absorption exhibited by RSAs is known to result from sequential single-photon absorption, and as such is an effective third-order optical nonlinearity to a first approximination.

For an RSA-material, the rate equations for a pulse travelling in the z-direction can be written (see the above references for details):

$$\frac{dI}{dz} = -I\alpha_{\rm nl} = -I(N_0\sigma_{10} + N_1\sigma_{21}) , \tag{14}$$

$$\frac{dN_0}{dt} = -N_0\sigma_{10}\frac{I}{\hbar\omega} + \frac{N_1}{\tau_{01}} , \tag{15}$$

$$N_1 = N_T - N_0 , \tag{16}$$

where the single-photon absorption cross sections are represented by the σ_{ji}; τ_{01} is the recombination time from the excited S_1 to the ground S_0 manifold; N_i are the populations of the singlet manifolds and N_T is the total molecular population. The critical condition for the onset of induced absorption is thus $R > 1$, where R is the ratio of the first excited-state to ground-state absorption cross section (σ_{21}/σ_{10}). Efficient RSA for picosecond pulses also requires that the recovery rate from the S_1 state is slow compared to the optical pumping rate, i.e., a recombination time τ_{01} which is much longer than the pulse duration τ_0.

Nonlinear refractive effects originate from the dye molecules and the solvent in which such a dye is dissolved. The change in the refractive index contains an instantaneous term and a term proportional to the accumulated material-excitation density [22] of the RSA material:

$$\Delta n(x, y, z', t) = n_2 I(x, y, z', t) + \sigma_n N_1(x, y, z', t) , \tag{17}$$

where σ_n represents the refractive index change per excitation per unit volume due to the generation of molecules (N_1) in the excited state.

Throughout our theoretical analysis, we solve the coupled rate equations in a self-consistent manner, together with the split-step BPM algorithm introduced earlier. This allows us to include all the refractive and absorptive nonlinear contributions and to account for the temporal and spatial profiles of the laser irradiance and for pulse depletion in the material.

For the simulations, the input irradiance profile is taken to be,

$$I = I_0\ f(t, r) = I_0 \exp\left[-\left(\frac{t}{\tau_0}\right)^2\right] \exp\left[-\left(\frac{2r}{\omega_0}\right)^2\right] , \tag{18}$$

where we use known experimental laser and sample parameters. Pulses of wavelength 532 nm, 15 ps duration and a spot size of 50 μm are assumed.

The modelled sample was taken to have a 1 cm path length, and the dye to have a molecular concentration of $6 \times 10^{16}\,\mathrm{cm}^{-3}$ in solution. The dye parameters correspond to the phthalocyanine CAP which is a fairly common RSA dye (see, for example, [33, 16]). Wei et al. [34] have shown, that the nonlinear refraction of this dye is dominated by the accumulated material-excitation density N_1 in the S_1 manifold. The instantaneous n_2 contribution is taken to arise from a Kerr effect in the solvent alone. The parameters for CAP were taken from the literature [22, 35, 36]. The ground-state absorption cross section σ_{10} was set equal to $3.4\times10^{-18}\,\mathrm{cm}^2$, the ratio of the excited-state to ground-state absorption cross sections R was set equal to 15, and the lifetime τ_{01} was 7 ns – corresponding to a typical dye recombination lifetime (see, for example, [36]) – which gives a long recovery of the nonlinear transmittance. The refractive cross section σ_n was taken to be $2.5 \times 10^{-22}\,\mathrm{cm}^3$. Solvents with different n_2 were used to investigate the influence of this parameter on the optical limiting.

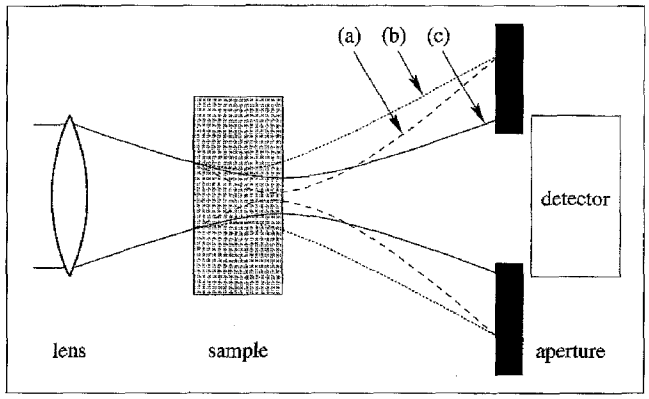

Fig. 6. Representation of a nonlinear optical limiter in the presense of (*a*) self-focusing, (*b*) self-defocusing, and for (*c*) linear propagation

The concept of enhanced limiting using refractive techniques is depicted in Fig. 6, showing detection through an aperture 10 cm behind the nonlinear material. The aperture diameter (1 mm) is sufficiently large to catch most of the low irradiance light (curve c); however, as the irradiances increase, induced absorptive effects cause a reduction of the transmittance and, in addition, nonlinear refractive effects distort the beam profile before it reaches the aperture, thus causing further transmittance reductions at the detector. In the self-focusing case (curve a), the beam is brought to a tighter focus and so diffraction is greater in the far field. For self-defocusing (curve b), the beam automatically diffracts more into the far field.

The results for self-focusing and self-defocusing, which include the above refractive and absorptive nonlinearities, are shown in Figs. 7a and 7b, respectively, where the output transmittance at the sample exit and the transmittance at the detector is calculated as a function of input fluence. As can be seen, the transmittance at the detector is greatly reduced in the presence of nonlinear refraction. For these simulations, solvents with n_2 equal to $\pm1.8 \times 10^{-14}\,\mathrm{W}^{-1}\mathrm{cm}^2$ were assumed. In the example given here, the instantaneous nonlinear refraction ($n_2 I$) is the dominant contribution. The case for self-focusing produces the greater enhanced limiting, but proves more difficult to simulate because catastrophic focusing occurs for high fluences.

For the defocusing simulation, the corresponding laser spatial profiles at a fluence of $3\,\mathrm{J/cm}^2$ are depicted in Figs. 8a and b. The former represents the field distribution at the sample exit, and the later corresponds to the field distribution at the aperture plane, which shows beautiful diffraction

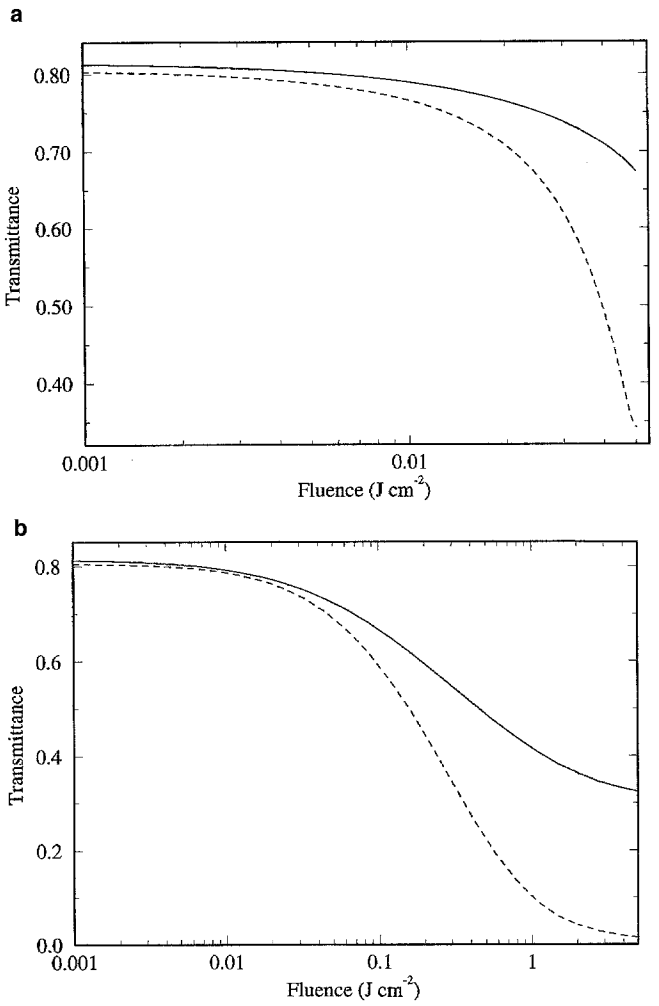

Fig. 7a,b. Simulated optical limiting transmittance curves in the presence of nonlinear absorption and nonlinear refraction. The *solid curve* corresponds to the case with absorption alone, and the *dashed curve* includes the effects of self-refraction, which is seen to reduce the transmittance (see text) for (**a**) positive and (**b**) negative nonlinear refractive index (n_2)

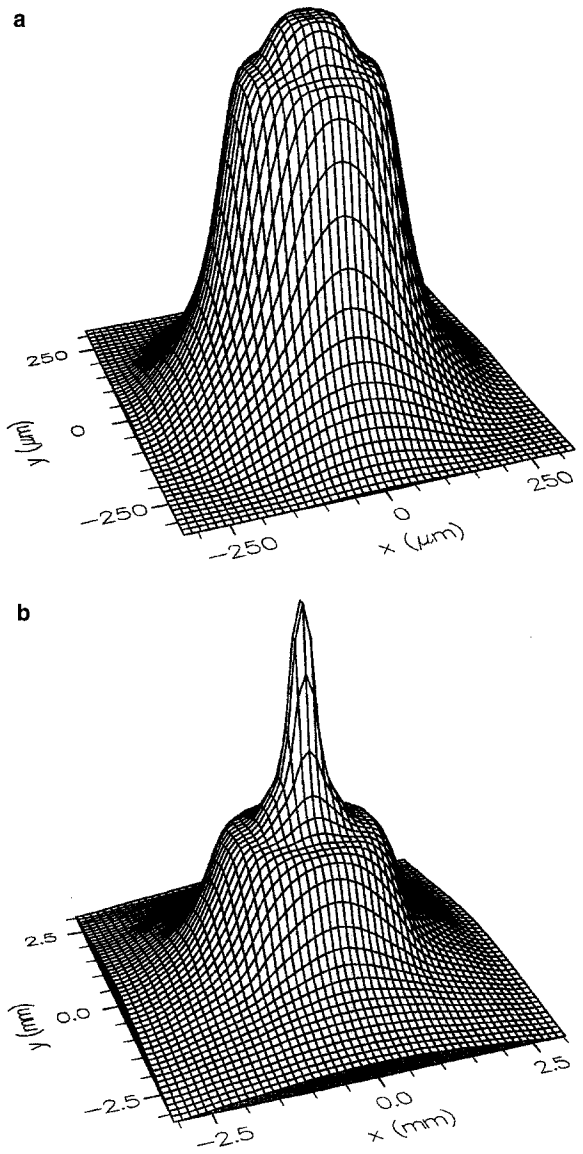

Fig. 8. a The laser spatial profile at the sample exit corresponding to the self-defocusing case in Fig. 7b for an input fluence of 3 J/cm^2. **b** Far-field spatial profile at 10 cm

patterns in the form of a bell with a concentric ring around the central spike.

In order to optimize the optical limiting, from an absorptive point of view alone, obviously one should increase the R value (excited-state to ground-state absorption cross section ratio) and lower the linear absorption coefficient. Also, the recovery rate from the S_1 manifold (τ_{01}) should be slow compared to the optical pumping rate. The role of nonlinear refraction is more subtle. We investigate for the defocusing case described above (Fig. 7b) at different nonlinear refractive indices n_2 and dye concentrations. One useful figure-of-merit is the 'contrast ratio', defined as the linear transmittance divided by the transmittance at the detector. Figures 9a and b plot the contrast ratio against the nonlinear refractive index n_2 for constant fluence levels of 0.3 J/cm^2, and 1 J/cm^2, respectively. The dye concentrations vary from 0 cm^{-3} (solid line) to 3×10^{17} cm^{-3} (dot-dashed line). At both fluence levels, the contrast ratio increases as the modulus of the nonlinear refractive index $|n_2|$ increases. The increase becomes flatter at higher dye concentrations. The absorption of the dye reduces the fluence of the light within the sample but also reduces the nonlinear refraction. As expected, the nonlinear absorption is the dominant effect of limiting if the nonlinear refractive index $|n_2|$ is small. Here, the best contrast ratio is achieved with high dye concentrations. For higher $|n_2|$ values, the refractive effect becomes the dominant mechanism giving the optimum contrast ratio at zero concentration, i.e., in a pure nonlinear solvent. The cross-over point between these two regimes moves to smaller $|n_2|$ at higher input fluence levels because the accumulative nonlinear absorption saturates but the instantaneous refractive effect does not. The higher fluence level (Fig. 9) also gives a better overall contrast ratio. In the simulations for Figs. 9a and b, the refractive cross section σ_n was set equal to zero to investigate pure instantaneous refractive effects only. For a material with negative σ_n, the nonlinear self-defocusing refractive effect becomes more pronounced

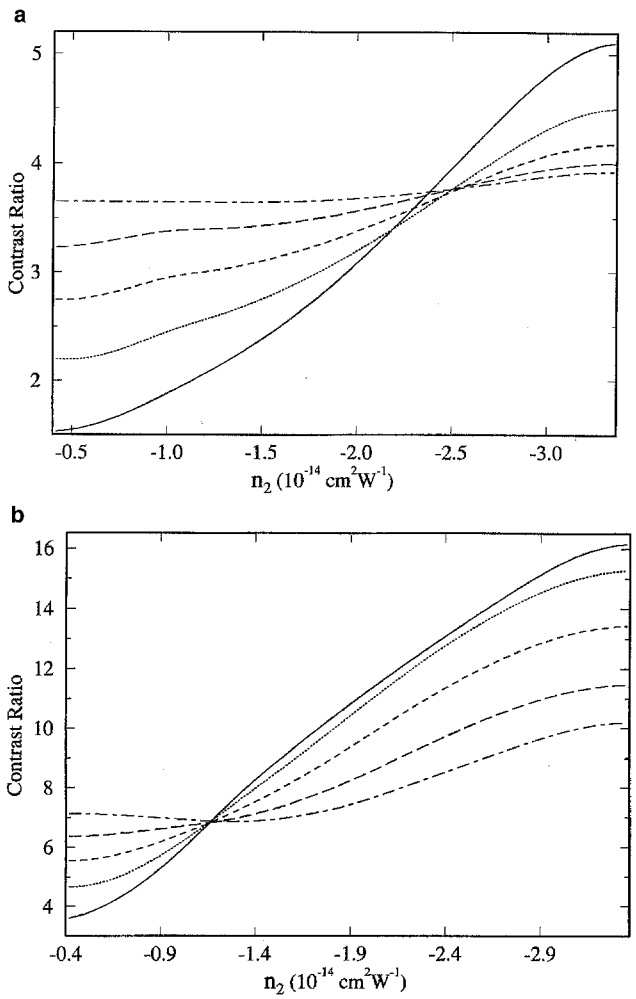

Fig. 9a,b. Contrast ratio (*see text*) for a range of dye concentrations and nonlinear refractive indices (n_2) values, for an input fluences of (**a**) 0.3 J/cm^2 and (**b**) 1 J/cm^2

and greater limiting is achieved. In the case of a positive σ_n, it becomes less pronounced as expected.

Further optimization of the optical-limiting device must account for any trade-off between contrast ratio and (linear) insertion loss. The point made here is that the BPM is a fast computational technique that can enable such optimization. Computational methods in this paper provide an efficient tool for the design of an optical limiter. An accurate simulation which includes nonlinear absorption and refraction contribution from both the solvent and dye takes typically only about one minute per data point on a SUN Sparc-Station 5 using a 128 × 128 computational grid, 10 time slices for the pulse, and 10 z-slices for the sample.

5 Conclusions

The BPM is described and adapted to model refractive effects of nonlinear materials for applications to power limiting and optical switching. A technique for far-field propagation from such nonlinear media – using a single FFT – is described, and its uses are shown for external propagation from such media. To demonstrate the strength of the technique, near- and far-field diffraction patterns arising from a triangular aperture were presented for both linear and nonlinear propagation.

Self-focusing and self-defocusing are shown to exhibit such effects as laser-beam trapping and beam division; the two separate profiles originate from an elliptical beam traversing an isotropic nonlinear medium. Finally, a passive optical limiter was simulated in the presence of both nonlinear absorption and nonlinear refraction, where the limiting was seen to be greatly enhanced for both the self-focusing and self-defocusing cases. The role of parameters for optical limiting are discussed.

The purpose of the paper was to demonstrate that the computational techniques applied are efficient enough to enable both fitting experimental results for thick samples, in order to determine the material parameters, and for modelling materials and configuration variations such as to optimize the experimental conditions.

Acknowledgements. J. M. Burzler would like to acknowledge financial support from the Studienstiftung Cusanuswerk. S. Hughes would like to acknowledge funding from the UK Engineering and Physical Science Research Council, and the Defence Research Establishment, Malvern. The authors are grateful to F. Haran from the Fibre Sensors Group at Heriot-Watt University for introducing them to the Beam Propagation Method (BPM) algorithm.

References

1. G. Wood, A. Mott, E. Sharp: SPIE Proc. **1692**, 1692 (1992)
2. J. Hermann: Opt. Quantum Electron. **19**, 169 (1987)
3. M. Sheik-Bahae, A. Said, D. Hagan, M. Soileau, E.W. Van Stryland: Opt. Eng. **30**, 1228 (1991)
4. A. Said, K. Mansour, J. Young, M. Soileau: SPIE Proc. **1105**, 103, 1989
5. W. Williams, M. Soileau, E.W. Van Stryland: Opt. Commun. **50**, 256 (1984)
6. I. Khoo, R. Lindquist, R. Michael, R. Mansfield, P. Zhou, P. Lopreti: SPIE Proc. **1307**, 336 (1990)
7. H.-P. Nolting, R. März: J. Lightwave Technol. **13**, 216 (1995)
8. T. Okoshi, S. Kitazawa: *Analysis methods for electromagnetic wave problems*, ed. by E. Yamashita (Artech House, Boston 1990) p. 341
9. J. Van Roey, J. Van der Donk, P. Laggase: J. Opt. Soc. Am. **71**, 803 (1981)
10. M. Munowitz, D. Vezzetti: Opt. Commun. **100**, 43 (1993)
11. L. Thylen: Opt. Quantum Electron. **15**, 433 (1983)
12. U. Trutschel, M. Mann, F. Lederer, C. Wachter, A.D. Boardman: Appl. Phys. Lett. **59**, 1940 (1991)
13. M. Mann, U. Trutschel, F. Lederer, L. Leine, C. Wachter: J. Opt. Soc. Am. **8**, 1612 (1991)
14. D. Harter, M. Shand, Y. Band: J. Appl. Phys. **56**, 865 (1984)
15. G. Allan, D. Labergerie, S. Rychnovsky, T. Boggess, A. Smirl, L. Tutt: J. Phys. Chem. **96**, 631 (1992)
16. J. Perry, L. Khundkar, D. Coulter, J. D. Alverez, S. Marder, T. Wei, M. Sence, E.W. Van Stryland, D. Hagan: *Organic Molecules for Nonlinear Optics and Photonics* (Kluwer, Dordrecht 1991) p. 369
17. D. Feit, J. Fleck: Appl. Opt. **17**, 3990 (1978)
18. M. Sheik-Bahae, H. Kwok: IEEE J. QE-**23**, 1974 (1987)
19. P. Murphy, N. Gallagher: J. Opt. Soc. Am. **73**, 1130 (1983)
20. D. Weaire, B.S. Wherrett, D. Miller, S. Smith: Appl. Opt. **4**, 331 (1979)
21. D. Bailey, P. Swarztrauber: SIAM J. Sci. Comput. **15**, 1105 (1994)
22. S. Hughes, J. Burzler, B. Wherrett: J. Opt. Soc. Am. B (in press)
23. P. Chapple, J. Staromlynska, R. McDuff: J. Opt. Soc. Am. B **11**, 975 (1994)
24. A. Snyder, L. Poladian, D. Mitchell: Opt. Lett. **17**, 267 (1992)
25. M. Sodha: Opt. Lett. **19**, 1110 (1994)

26. B. Gross, J. Manassah: Phys. Lett. A **169**, 371 (1992)
27. P. Ho, R. Alfano: Phys. Rev. A **20**, 2170 (1979)
28. T. Harvey, W. Ji, A. Kar, B. Wherrett: Opt. Lett. **15**, 408 (1990)
29. E.W. Van Stryland, H. Vanherzeele, M. Woodall, A. Smirl, S. Guha, T. Boggess: Opt. Eng. **24**, 613 (1985)
30. M. Joshi, S. Mishra, H. Rawat, S. C. Mehendale, K. C. Rustagi: Appl. Phys. Lett. **62**, 1763 (1993)
31. K. Reddy: Opt. Quantum Electron. **19**, 203 (1987)
32. J. Faure, J. Fouassier, D. Lougnot: In 27th Int'l Meeting Soc. Chem. Phys. **18**, 263 (1976)
33. D. Coulter, V. Miskowski, J. Perry, T. Wei, E.W. Van Stryland, D. Hagan: SPIE Proc. **1105**, 42 (1989)
34. T. Wei, D. Hagan, M. Sence, E.W. Van Stryland, J. Perry, D. Coulter: Appl. Phys. B **54**, 46 (1992)
35. E.W. Van Stryland, M. Sheik-Bahae, A. Said, D. Hagan: SPIE Proc. **1852**, 135 (1993)
36. S. Speiser, N. Shakkour: Appl. Phys. B **38**, 191 (1985)

This article was processed by the author using the LaTeX style file *pljour2* from Springer-Verlag.